



**HAL**  
open science

## Improvement of thermoelectric performance in Sb<sub>2</sub>Te 3 / Te composites

Subarna Das, P. Singha, Ramzy Daou, Oleg I Lebedev, Sylvie Hébert,  
Antoine Maignan, Aritra Banerjee

► **To cite this version:**

Subarna Das, P. Singha, Ramzy Daou, Oleg I Lebedev, Sylvie Hébert, et al.. Improvement of thermoelectric performance in Sb<sub>2</sub>Te<sub>3</sub> / Te composites. *Physical Review Materials*, 2022, 6 (3), pp.035401. 10.1103/PhysRevMaterials.6.035401 . hal-03822185

**HAL Id: hal-03822185**






**<https://hal.science/hal-03822185v1>**

Submitted on 20 Oct 2022

**HAL** is a multi-disciplinary open access archive for the deposit and dissemination of scientific research documents, whether they are published or not. The documents may come from teaching and research institutions in France or abroad, or from public or private research centers.

L'archive ouverte pluridisciplinaire **HAL**, est destinée au dépôt et à la diffusion de documents scientifiques de niveau recherche, publiés ou non, émanant des établissements d'enseignement et de recherche français ou étrangers, des laboratoires publics ou privés.

## Improvement of thermoelectric performance in $\text{Sb}_2\text{Te}_3/\text{Te}$ composites

Subarna Das <sup>1</sup>, P. Singha <sup>1</sup>, Ramzy Daou,<sup>2</sup> Oleg I. Lebedev,<sup>2</sup> Sylvie Hébert <sup>2</sup>,  
Antoine Maignan <sup>2</sup> and Aritra Banerjee <sup>1,3,\*</sup>

<sup>1</sup>Department of Physics, University of Calcutta, 92 A P C Road, Kolkata 700 009, India

<sup>2</sup>Laboratoire de Cristallographie et Sciences des Matériaux (CRISMAT), Normandie Université, UMR6508 CNRS, ENSICAEN, UNICAEN, 14000 Caen, France

<sup>3</sup>Center for Research in Nanoscience and Nanotechnology, University of Calcutta, JD-2, Sector-III, Saltlake, Kolkata 700 106, India



(Received 17 October 2021; accepted 18 February 2022; published 4 March 2022)

Te-impurity-incorporated  $\text{Sb}_2\text{Te}_3$ , i.e.,  $\text{Sb}_2\text{Te}_3 + x \text{ mol } \% \text{ Te}$  ( $x = 0, 4, 6$ , and  $9$ ) composites were synthesized by solid-state reaction technique. Analysis of x-ray diffraction indicates not only Te impurity as a second phase but also doping of Te via suppression of inherent Te vacancies in the  $\text{Sb}_2\text{Te}_3$  matrix. As a result of this doping and of the change in formation energy of different types of native defects in  $\text{Sb}_2\text{Te}_3$  due to synthesis in a Te-rich condition, carrier concentration ( $n_{\text{H}}$ ) lower than the pristine sample was observed. Low  $n_{\text{H}}$  along with gradual convergence of valence bands due to progressive suppression of Te vacancies increases the Seebeck coefficient ( $S$ ) in Te-incorporated samples. Even though Te impurities increase electrical resistivity ( $\rho$ ), enhanced texturing of lattice planes ensures that charge carrier mobility does not degrade due to Te addition. As a result, a maximum power factor  $= 17 \mu\text{W cm}^{-1} \text{K}^{-2}$  at  $T = 480 \text{ K}$  for  $x = 6$  has been achieved. In addition, Te addition strengthens phonon scattering via an increase of phonon-phonon Umklapp scattering and point-defect-induced scattering of phonons. Due to such a strong phonon scattering, thermal conductivity ( $\kappa$ ) decreases, and a reduced lattice thermal conductivity ( $\kappa_{\text{L}}$ ), as low as  $0.28 \text{ W m}^{-1} \text{K}^{-1}$  at  $500 \text{ K}$  for  $x = 6$ , has been achieved. As a result of simultaneous increase of  $S$  and decrease of  $\kappa$ , a high  $ZT \sim 0.87$  at  $480 \text{ K}$ , almost 33% higher than that of the host material, has been achieved.

DOI: [10.1103/PhysRevMaterials.6.035401](https://doi.org/10.1103/PhysRevMaterials.6.035401)

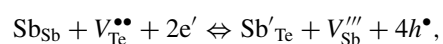
### I. INTRODUCTION

Thermoelectric (TE) material, despite being promising as a potential candidate to convert waste heat to electricity and vice versa, is still mostly used for niche applications like spacecraft and the defense industry [1,2]. Strong coupling among intrinsic material properties like the Seebeck coefficient ( $S$ ), electrical resistivity ( $\rho$ ), and the electronic component of thermal conductivity ( $\kappa_e$ ) via carrier concentration ( $n_{\text{H}}$ ) makes it challenging to obtain TE material of high efficiency, defined by the dimensionless figure of merit  $ZT = S^2T/\rho\kappa$ , where  $T$  is the absolute temperature,  $\kappa$  ( $= \kappa_e + \kappa_{\text{L}}$ ) is the thermal conductivity, and a significant part of  $\kappa$  originates from lattice contribution ( $\kappa_{\text{L}}$ ) [1–3]. In recent times, two main strategies have generally been adopted for increasing  $ZT$ : one is to decouple these parameters to increase the power factor (PF  $= S^2/\rho$ ) by band engineering which includes band distortion [4], band convergence [5,6], band nestification [7], and the other involving efforts to reduce  $\kappa_{\text{L}}$  by phonon engineering [8].

Simultaneous attempts to tune  $n_{\text{H}}$  of well-known TE materials by manipulating its intrinsic defects and introducing a suitable second phase in them via synthesizing composites can be an effective route to achieve high  $ZT$  [9]. In such multiphase structures, enhanced  $S$  is often obtained via the carrier energy filtering effect due to band bending at the interface between host TE material and the second phase [10]. Scatter-

ing of phonons at the heterointerfaces and by extrinsic defects created due to the incorporation of a second phase should also decrease  $\kappa$  [11–13]. However, it can have a negative impact on carrier mobility ( $\mu$ ). It should be mentioned here that the improvement of  $ZT$  can be realized through a more significant reduction of  $\kappa$  than  $\mu$  [14]. High  $\mu$  can be maintained through inducing enhanced texture in the multiphase structures compared with its host material [15–17].

$\text{Sb}_2\text{Te}_3$ -based solid solutions are well known for their potential TE application around room temperature [18–20], which are used for constructing thermogenerators and solid-state coolers [21]. Narrow bandgap ( $E_g \sim 0.28 \text{ eV}$ ) [13] along with layered structure make them suitable as TE material. Furthermore, realization of  $\text{Sb}_2\text{Te}_3$  as a three-dimensional topological insulator in recent years has enhanced the potential of the system from an application point of view [22]. Detrimental TE performance of this material at elevated temperature results from its small bandgap, which makes it easy for minority carriers to get thermally activated. This induces bipolar effect which not only decreases  $S$  but also introduces additional  $\kappa$ , leading to lower  $ZT$  [13]. Overall increase of the majority carrier can prevent this bipolar effect and help  $\text{Sb}_2\text{Te}_3$  to achieve higher  $ZT$  beyond room temperature [14]. Intrinsic defects play a major role in determining the  $n_{\text{H}}$  of the material. The  $n_{\text{H}}$  of  $\text{Sb}_2\text{Te}_3$ , where Sb and Te are in stoichiometric amount during synthesis, is governed by the interplay between antisite defects and vacancies formed during crystal growth [23]:



\*Corresponding author: arbphy@caluniv.ac.in

where  $V_{\text{Te}}^{\bullet\bullet}$  and  $V_{\text{Sb}}^{\prime\prime\prime}$  are the Te and Sb vacancies,  $\text{Sb}_{\text{Te}}^{\prime}$  is the antisite defects,  $e^{\prime}$  and  $h^{\bullet}$  are electron and hole, respectively. First-principles calculations suggest that, during synthesis of  $\text{Sb}_2\text{Te}_3$  under Te-rich condition, formation energy ( $E$ ) of cation vacancy ( $V_{\text{Sb}}^{\prime\prime\prime}$ ) is lowest among all defects, i.e.,  $E(V_{\text{Sb}}^{\prime\prime\prime}) < E(\text{Sb}_{\text{Te}}^{\prime}) < E(V_{\text{Te}}^{\bullet\bullet})$  [24]. Hence, in such conditions, concentration of  $V_{\text{Sb}}^{\prime\prime\prime}$ , which dopes electrons, increases [24]. Under Te-rich condition, since  $E(V_{\text{Te}}^{\bullet\bullet})$  is highest, the presence of extra Te during the synthesis lowers the concentration of the hole dopant  $V_{\text{Te}}^{\bullet\bullet}$ . Thus, simultaneous increase of  $V_{\text{Sb}}^{\prime\prime\prime}$  and decrease of  $V_{\text{Te}}^{\bullet\bullet}$  lead to lower hole carrier concentration ( $n_{\text{H}}$ ), which is favorable to obtain higher  $S$ . Furthermore, such additional Te can create extrinsic point defects in the  $\text{Sb}_2\text{Te}_3$  matrix and scatter high-frequency phonons.

At the same time, TE performance of  $\text{Sb}_2\text{Te}_3$  has been increased by introducing a second phase into the system. Ko *et al.* [25] have reported higher PF through Pt incorporation in  $\text{Sb}_2\text{Te}_3$  due to an enhanced  $S$  via carrier energy filtering.  $\kappa$  value as low as  $\sim 0.14 \text{ W m}^{-1} \text{ K}^{-1}$  in the temperature range 300–523 K and  $ZT \sim 1.18$  at 523 K has been achieved in  $p$ -type  $\text{Sb}_2\text{Te}_3/\text{poly}(3,4\text{-ethylenedioxythiophene})$  sample [26]. It is reported that  $\text{Ag}_x\text{Te}_y$  addition has led to  $\sim 50\%$  higher TE performance than pristine  $\text{Sb}_2\text{Te}_3$  [27]. Lee *et al.* [28] have obtained high  $ZT \sim 1.5$  at 700 K in  $\text{Sb}_2\text{Te}_3/\text{Ag}_2\text{Te}$  through increasing  $S$  and lowering  $\kappa$ . Furthermore, an enhanced TE performance has been accomplished by including Sb as second phase in  $\text{Sb}_2\text{Te}_3$  through increased phonon scattering together with carrier filtering by potential barriers at the Sb/ $\text{Sb}_2\text{Te}_3$  interface [29]. Despite all such reports, the simultaneous attempt of manipulating  $n_{\text{H}}$  via native defect engineering and introducing second phase in  $\text{Sb}_2\text{Te}_3$  has not been explored yet. Elemental Te, having nested band structure at the  $H$  point, has attracted increasing attention in the field of TE research. Its high number of degenerate hole pockets enhances density of states effective mass, which in turn gives rise to high  $S$  ( $\sim 400 \mu\text{V/K}$  at 300 K) [30,31]. These properties, along with its ability to alter  $n_{\text{H}}$  of  $\text{Sb}_2\text{Te}_3$ , makes Te a suitable material for synthesizing  $\text{Sb}_2\text{Te}_3$ -based multiphase structure, i.e.,  $\text{Sb}_2\text{Te}_3/\text{Te}$ . In this paper, a detailed investigation of the TE properties of  $\text{Sb}_2\text{Te}_3/\text{Te}$  structure, having different mole percentage than Te, is reported. X-ray diffraction (XRD) patterns indicate doping of Te in the  $\text{Sb}_2\text{Te}_3$  matrix for the  $\text{Sb}_2\text{Te}_3/\text{Te}$  samples, which is further confirmed by lowering of  $n_{\text{H}}$  in the samples. Lower  $n_{\text{H}}$ , along with favorable carrier effective mass, increases  $S$ . An attempt has been made to estimate energy offset between multicarrier valence bands and observe its effect on  $S$ . With increasing Te addition, a gradual convergence of valence bands is predicted, which helps to increase  $S$  in the synthesized system. Te incorporation introduces a preferred crystallographic orientation of the samples, which helps to maintain  $\mu$ . The  $\kappa$  decreases with Te addition, and the lowest  $\kappa \sim 0.91 \text{ W m}^{-1} \text{ K}^{-1}$  at 500 K has been accomplished. As a result, the highest  $ZT \sim 0.87$  at 480 K, almost 33% higher than the host material, has been achieved in  $\text{Sb}_2\text{Te}_3/\text{Te}$  samples.

## II. EXPERIMENTS

$\text{Sb}_2\text{Te}_3/\text{Te}$  composite samples, i.e.,  $\text{Sb}_2\text{Te}_3 + x \text{ mol } \% \text{ Te}$  ( $x = 0, 4, 6, \text{ and } 9$ ) were synthesized by solid-state reaction

technique. Suitable amounts of elemental Sb and Te (Alfa Aesar 99.999%) were taken and vacuum sealed in quartz ampoules under  $10^{-3} \text{ Pa}$  pressure. It was annealed at 1123 K for 24 h followed by a controlled cooling down to 893 K at 5 K/h. After subsequent sintering at 893 K for 96 h, it was finally quenched in liquid nitrogen. The resulting ingots were powdered using an agate mortar and pestle. Thereafter, the phase of the samples was confirmed by XRD technique (Model: X'Pert Powder, PANalytical) by illuminating the sample by Cu- $K_{\alpha}$  radiation (wavelength = 0.15418 nm). Standard Si was used to determine the instrumental profile [32]. Rietveld refinement using Materials Analysis Using Diffraction software was performed for detailed structural analysis [33]. In this analysis, the microstructural refinement is performed according to the formalism of Popa [34], which is capable of modeling isotropic and anisotropic size and strain broadening. To determine the degree of preferred orientation, the March-Dollase approach is used in Rietveld analysis [35]. Transmission electron microscopy (TEM) was performed using JEM ARM200F cold FEG probe and image-aberration-corrected microscope, operated at 200 kV and equipped with a large-angle CENTURIO energy-dispersive x-ray (EDX) detector, Orius Gatan CCD camera, and Quantum GIF. The TEM samples were prepared in the conventional way: depositing a solution of the material and ethanol on a carbon holey Cu grid. The powders of the synthesized samples were pressed into cylindrically shaped pellets of 10 mm diameter  $\times$  2 mm height by applying a pressure of 60 kPa through a hydraulic press for 10 min at room temperature. Density measurements by the Archimedes method reveal that all pellets are of  $\sim 95\%$  of their theoretical density. Temperature dependence of carrier concentration  $n_{\text{H}}(T)$  was estimated by performing Hall measurements at 5–300 K using Physical Property Measurement System (PPMS-9T, Quantum Design, Inc) with the magnetic field being perpendicular to the flow of current. For Hall measurements at each temperature, the Hall voltage was collected at different magnetic fields from 9 to  $-9$  T. The  $n_{\text{H}}$  at a particular temperature was calculated from the slope of Hall voltage vs magnetic field data. High temperature (300–480 K)  $S(T)$  and  $\rho(T)$  were simultaneously measured in UlvacRiko ZEM3 measuring system on parallelepiped pellet samples of  $3 \times 2 \times 8 \text{ mm}^3$ . In the interval 300–500 K,  $\kappa(T)$  was estimated using the formula:  $\kappa(T) = \text{specific heat} \times \text{diffusivity} \times \text{density}$ . Specific heat  $C_p$  was taken equal to the Dulong-Petit value ( $124.5 \text{ J mol}^{-1} \text{ K}^{-1}$ ). As mentioned earlier, density is  $\sim 95\%$  of the respective theoretical density. Diffusivity measurements were performed by Netzsch 457 microflash laser flash system on a pellet of  $2 \times 6 \times 6 \text{ mm}^3$ . Inert atmosphere (either partial helium pressure or dynamic vacuum) was maintained for carrying out all measurements.

## III. RESULTS AND DISCUSSIONS

### A. Evidence for the composite nature of the samples

Structural characterization of the as-prepared  $\text{Sb}_2\text{Te}_3/\text{Te}$  samples by XRD (Fig. 1) confirms a pure single phase for the pristine  $\text{Sb}_2\text{Te}_3$  ( $x = 0$ ) sample (JCPDS Card No. 71-0393). However, for samples having Te inclusion, i.e.,  $x = 4, 6, \text{ and } 9$  in  $\text{Sb}_2\text{Te}_3 + x \text{ mol } \% \text{ Te}$ , some extra peaks around

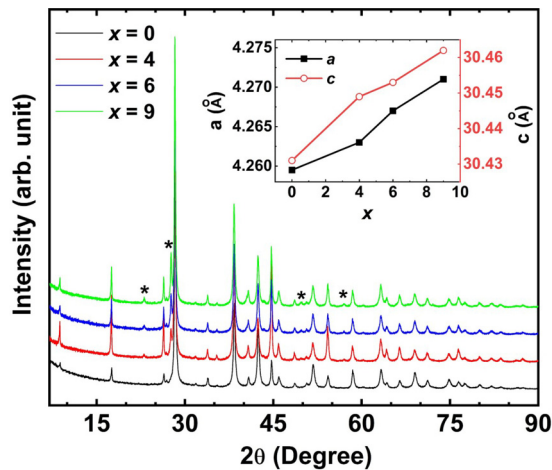


FIG. 1. Room temperature x-ray diffraction (XRD) patterns for  $\text{Sb}_2\text{Te}_3 + x$  mol % Te ( $x = 0, 4, 6,$  and  $9$ ) composite samples. XRD peaks which appeared due to the presence of elemental Te in  $x = 4, 6,$  and  $9$  are marked with asterisks (\*). Inset: Variation of lattice parameters (i.e.,  $a$  and  $c$ ) of  $\text{Sb}_2\text{Te}_3$  with increasing Te incorporation. Estimated errors in the refined lattice parameters are within the size of the data points and are provided in Fig. SM1 in the Supplemental Material [36]. The lines joining the data points are guidelines for the eye.

$2\theta = 23.10^\circ, 27.57^\circ, 49.67^\circ,$  and  $56.96^\circ$  in addition to the diffraction peaks of  $\text{Sb}_2\text{Te}_3$  (i.e.,  $x = 0$  sample) appear in the XRD patterns. These peaks can respectively be indexed as the (100), (011), (201), and (022) lattice planes of Te (JCPDS Card No. 79-0736), which indicates the presence of elemental Te as a second phase in these samples. The structural parameters of the samples are extracted by Rietveld refinement and presented in the Supplemental Material [36]. The diffraction peaks of  $\text{Sb}_2\text{Te}_3$  and Te are indexed with rhombohedral ( $R\bar{3}m$ ) and hexagonal ( $P3_121$ ) crystal structures, respectively. The structural refinements show that lattice parameters of  $\text{Sb}_2\text{Te}_3$  ( $a$  and  $c$ ) increase with increasing  $x$  (inset: Fig. 1). This implies the formation of  $\text{Sb}_2\text{Te}_3/\text{Te}$  composite with a doping effect in the  $\text{Sb}_2\text{Te}_3$  majority phase along with the presence of the minority Te one. It is noteworthy to mention here that the  $\text{Sb}_2\text{Te}_3$  unit cell is made of three quintuple layers (QLs) of Sb and Te interconnected with one another by weak van der Waals forces. Each QL is comprised of Te1-Sb-Te2-Sb-Te1 stacking, where Te1 and Te2 denote two types of differently bonded Te atoms [18]. For refinement of Te-incorporated samples, i.e.,  $x = 4, 6,$  and  $9$ , texture along the (006), (009), and (0015) lattice planes of  $\text{Sb}_2\text{Te}_3$  are considered. Our Rietveld refinement data indicate that, with increasing  $x$ , occupancy of Te2 site increases. To be precise, Te2 occupancy increases from 0.980 to 0.992 when  $x$  increases from 0 to 9. The grain size does not change significantly with Te addition and hovers  $\sim 30\text{--}40$  nm on average for all samples. Furthermore, Rietveld refinement parameters, as indicated in Fig. SM1 in the Supplemental Material [36], demonstrate that lattice strain increases with Te incorporation, which plausibly suggests the existence of a compressive pressure on the  $\text{Sb}_2\text{Te}_3$  matrix due to the presence of Te as second phase [37]. Moreover, an attempt has been made to extract the phase fraction of  $\text{Sb}_2\text{Te}_3$  and Te

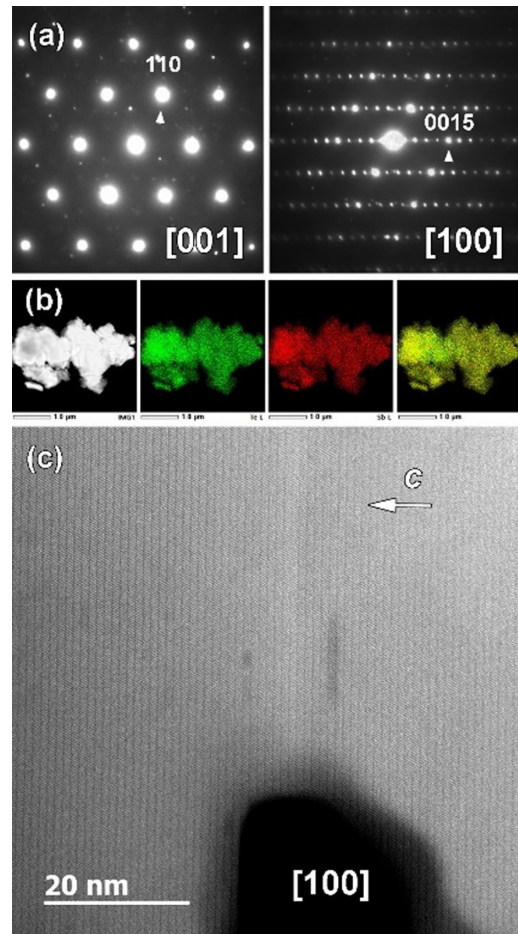


FIG. 2. (a) Electron diffraction (ED) patterns collected along main zone axis indexed based on rhombohedral ( $R\bar{3}m$ )  $\text{Sb}_2\text{Te}_3$  structure. (b) Low-magnification high-angle annular dark-field (HAADF) scanning transmission electron microscopy (STEM) image and simultaneously acquired energy-dispersive x-ray (EDX)-STEM elemental mapping for Te L, Sb L, and overlaid color image. (c) Middle-magnification [100] HAADF-STEM image of single  $\text{Sb}_2\text{Te}_3$  crystallite.

impurity (Table SM1 in the Supplemental Material [36]) via analyzing the intensity profile of XRD data. It is revealed that, for  $x = 4, 6,$  and  $9$ , the phase fractions of Te impurity present in the samples are  $\sim 5.1, 6.9,$  and  $9.5$  mol %, respectively. Thus, XRD analysis clearly implies that Te is not only present in the  $\text{Sb}_2\text{Te}_3/\text{Te}$  samples as a separate phase but also has some doping effect on the host matrix.

To check the microstructure of the  $\text{Sb}_2\text{Te}_3/\text{Te}$  composite and localize the excess of Te, TEM, including electron diffraction (ED), high-angle annular dark-field scanning TEM (HAADF-STEM), and EDX-STEM elemental mapping of  $x = 0$  and  $6$  samples were performed. ED patterns of the  $x = 6$  sample collected along the main zone axis [Fig. 2(a)] confirmed rhombohedral  $\text{Sb}_2\text{Te}_3$  ( $R\bar{3}m$ ) structure with the following unit cell parameters:  $a = 0.427$  nm and  $c = 3.047$  nm. EDX elemental mapping in STEM mode [Fig. 2(b)] and middle-magnification HAADF-STEM imaging show structure and chemical perfections: structure free of extended defects and homogeneous distribution of all elements at the

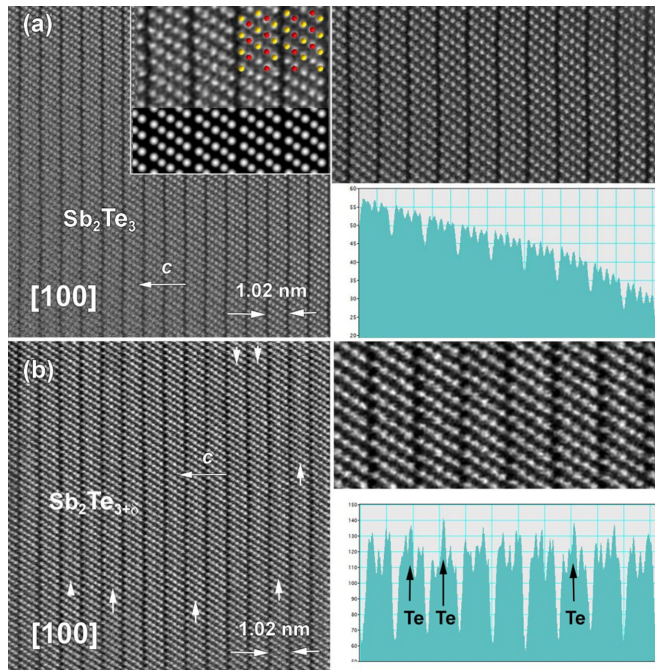


FIG. 3. (a) Left panel: High-resolution [100] high-angle annular dark-field (HAADF) scanning transmission electron microscopy (STEM) image of  $\text{Sb}_2\text{Te}_3$  structure. The magnified experimental image with overlaid simulated image and structural model is given as the inset, where Sb is red and Te yellow. Right panel: The magnified high-resolution HAADF-STEM image and corresponding intensity line scan profile along the  $c$  axis. (b) Left panel: High-resolution [100] HAADF-STEM image of  $\text{Sb}_2\text{Te}_{3+\delta}$  structure. The white arrows depict the atomic layers with an enhanced contrast. Right panel: The magnified high-resolution HAADF-STEM image and corresponding intensity line scan profile along the  $c$  axis. The maximum intensity peaks (marked with black arrows) correspond to Te-rich atomic layers.

nanoscale level [Fig. 2(c)]. The quantitative analysis of EDX data confirms the excess of Te and gives a ratio for  $\text{Sb}_2\text{Te}_{3+\delta}$  in the  $x = 6$  sample as the following:  $\text{Te}/\text{Sb} = 62/38$  at. %.

Moreover, the careful analysis of high-resolution HAADF-STEM images of the  $\text{Sb}_2\text{Te}_3$  sample with nominal composition [ $x = 0$ , Fig. 3(a)] and  $\text{Sb}_2\text{Te}_{3+\delta}$  [ $x = 6$ , Fig. 3(b)] along the [100] zone axis reveals an enhanced contrast for some atomic layers in  $\text{Sb}_2\text{Te}_{3+\delta}$  [Fig. 3(b), marked by white arrows] with respect to  $\text{Sb}_2\text{Te}_3$  [Fig. 3(a)], where all layers exhibit similar contrast [see inset line scan profile in Fig. 3(a)] as well as in the simulated image [Fig. 3(a), left panel inset]. Bearing in mind that contrast in the HAADF-STEM image is proportional to atomic number ( $\sim Z^2$ ) and thickness of the sample, it is impossible to distinguish Sb (51) and Te (52) so that Sb and Te layers have identical contrast. However, the intensity line scan profile [Fig. 3(b), right panel] clearly demonstrates an increase of the contrast of some of the Sb-Te layers. According to the structural model overlaid on a high-resolution HAADF-STEM image [Fig. 3(a), left panel inset], these layers correspond to Te layers, suggesting the presence of Te-rich layers with respect to the other layers within the  $\text{Sb}_2\text{Te}_{3+\delta}$  structure.

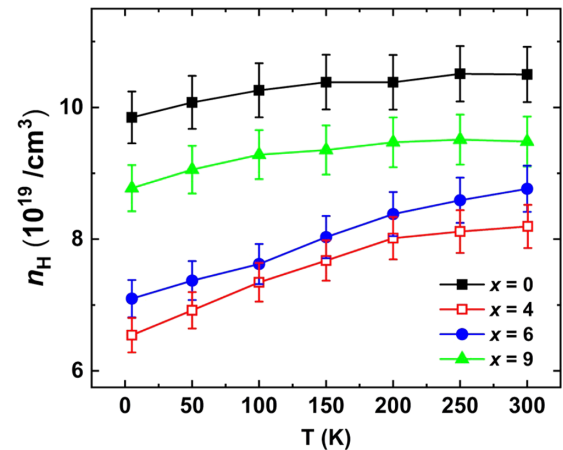


FIG. 4. Thermal variation of carrier concentration ( $n_H$ ) for different mole percentage ( $x$ ) of Te in  $\text{Sb}_2\text{Te}_3/\text{Te}$  samples. Lines connecting the data points are provided as a guide to the eye.

### B. Consequence on the $\text{Sb}_2\text{Te}_3$ doping level: Hall effect and Seebeck coefficient

As shown in the structural part, the extra Te present at the Te2 crystallographic site of  $\text{Sb}_2\text{Te}_3$  is expected to lower the concentration of inherently present Te vacancy  $V_{\text{Te}}^{\bullet\bullet}$ . To ensure that a doping effect occurs,  $n_H(T)$  of the samples was measured. The positive slope of Hall voltage vs magnetic field (not shown) suggests that the  $n_H$  data reported here correspond to hole concentration. Moreover,  $n_H$  decreases with Te incorporation (Fig. 4), at 300 K, from  $n_H = 1.05 \times 10^{20}/\text{cm}^3$  down to  $n_H = 9.50 \times 10^{19}/\text{cm}^3$  for the pristine  $\text{Sb}_2\text{Te}_3$  and  $x = 9$  samples, respectively. However, the lowest value of  $n_H (= 9.50 \times 10^{19}/\text{cm}^3)$  at 300 K is obtained for  $x = 4$  (discussed later).

Such changes in the charge carrier concentration affect also the Seebeck coefficient, as observed in Fig. 5 which displays the temperature-dependent Seebeck coefficient  $S(T)$  of the samples. The positive sign of  $S$  indicates that all the samples are  $p$  type in nature, which corroborates with our  $n_H$  data. Monotonic increase of  $S$  throughout the whole temperature range and an almost linear regime for  $T > 300$  K can be

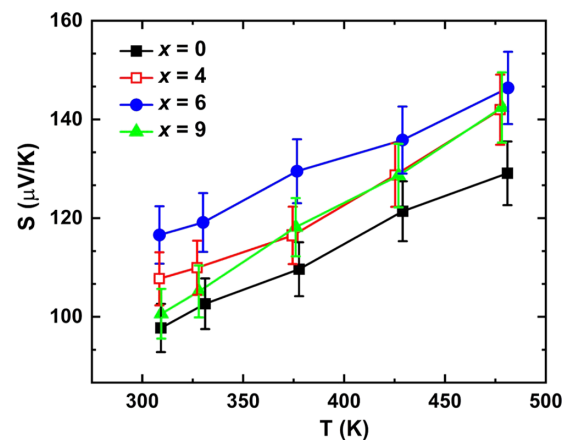


FIG. 5. Thermal variation of the Seebeck coefficient  $S$  for  $\text{Sb}_2\text{Te}_3/\text{Te}$  samples. The lines joining the data points are guidelines for the eye.

related to classical behavior of  $S(T)$ , where  $S$  is expressed by the simple semiclassical Mott-Jones formula of electron transport [1]:

$$S = \frac{8\pi^2 k_B^2 T}{3eh^2} m^* \left( \frac{\pi}{3n_H} \right)^{2/3}, \quad (1)$$

where  $k_B$ ,  $e$ ,  $h$ , and  $m^*$  are the Boltzmann constant, electron charge, Planck constant, and effective mass, respectively. For pristine  $\text{Sb}_2\text{Te}_3$ , the  $S$  value reaches  $129 \mu\text{V/K}$  at 480 K, which is one of the highest  $S$  reported for the pristine bulk polycrystalline  $\text{Sb}_2\text{Te}_3$  system [12,23,27,28,38,39]. The room temperature value of  $S$  ( $\sim 102 \mu\text{V/K}$ ) obtained in this case for the pristine sample matches very well with the existing reported data [40,41]. In addition, usually a peak in  $S(T)$  data  $\sim 350$  K has been reported in the literature for this system. Researchers ascribed this peak to activation of the minority carrier, which subdues the contribution from majority carriers (holes) [41]. Absence of such a peak in our case can be explained by higher hole concentration in the present system. The trend, as can be obtained from extrapolation of  $n_H(T)$  data (Fig. 4), indicates that the  $n_H$  values in the high-temperature regime ( $>300$  K) are considerably higher than in the literature [12,14,27,42]. For the  $\text{Bi}_{0.5}\text{Sb}_{1.5}\text{Te}_3$ -based system, Witting *et al.* [14] have also attributed the shifting of the peak in  $S(T)$  data toward high  $T$  to higher  $n_H$ . In the synthesized composite samples reported here, majority carriers dominate the  $S(T)$  data, and the contribution of minority carriers (electron here) at high temperature is overwhelmed by majority carriers, which is manifested in the monotonic increase of  $S(T)$  data up to the highest measurement temperature. With the inclusion of Te,  $S$  increases up to  $x = 6$  and then decreases for  $x = 9$ . The highest  $S$  value of  $146 \mu\text{V/K}$  at 480 K is measured for  $x = 6$ . Such a trend of  $S$  with  $x$  mostly follows from the variation of  $n_H$  with Te incorporation and can be explained by Eq. (1). However, the highest  $S$  for  $x = 6$  despite not having the lowest  $n_H$  can be understood by a nonmonotonic change of  $m^*$  with  $x$  (discussed later).

### C. TE PF = $S^2/\rho$

Figure 6(a) depicts the temperature variation of the electrical resistivity  $\rho$ . Monotonic increase of  $\rho$  with temperature indicates metallic behavior for all the samples in the temperature range of measurement. The room-temperature  $\rho$  value of pristine  $\text{Sb}_2\text{Te}_3$  is in good agreement with the literature data [43,44]. Te addition increases  $\rho$ . Samples with  $x = 4$  and 6 having almost the same  $n_H$  possess a similar  $\rho$  value. Here,  $\rho$  can be expressed as:  $\rho = 1/n_H e \mu$ . Increase of  $\rho$  for  $x = 4$  and 6 having almost the same  $\mu$  as  $x = 0$  (shown later) can be attributed to the lower  $n_H$  of the samples. Although  $n_H$  increases with further inclusion of Te,  $\rho$  becomes maximum for  $x = 9$  among all samples. This can be caused by a significant decrease of  $\mu$  for the sample (shown later).

PF, estimated using  $S(T)$  and  $\rho(T)$  data, is depicted in Fig. 6(b). PF increases with temperature and saturates  $\sim 400$  K [Fig. 6(b)]. In the temperature range of measurement, the highest PF is observed for  $x = 6$ , which corroborates with  $S(T)$  data. This sample reports  $\sim 15\%$  increase in PF value at 480 K (highest temperature measured) as compared with the pristine  $\text{Sb}_2\text{Te}_3$  sample.

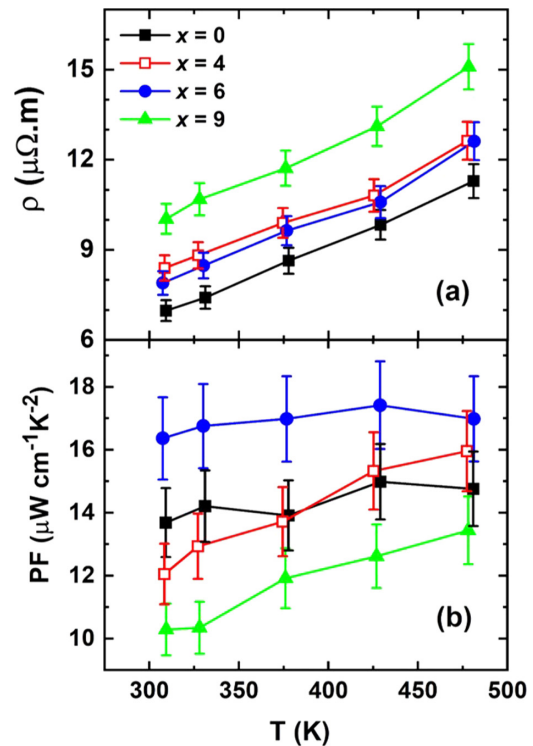


FIG. 6. Temperature dependent (a) electrical resistivity  $\rho$  and (b) power factor (PF) of all Te-impurity-incorporated  $\text{Sb}_2\text{Te}_3$  samples. Lines connecting the data points are provided as guides to the eye.

### D. Thermal conductivity

To investigate the temperature dependence of thermal conduction and relevant phonon dynamics in the samples,  $\kappa(T)$  was measured. As depicted in Fig. 7(a),  $\kappa$  decreases monotonically with increasing temperature for all samples. It is observed that Te incorporation leads to decrease in  $\kappa$ . The lowest  $\kappa$  is obtained for the  $x = 6$  sample, with a minimum value of  $0.92 \text{ Wm}^{-1} \text{ K}^{-1}$  at 500 K. As compared with its pristine counterpart, the maximum decrease of  $\sim 14\%$  in  $\kappa$  is observed for the  $x = 6$  sample. Such a low  $\kappa$  value is one of the lowest  $\kappa$  reported so far for  $\text{Sb}_2\text{Te}_3$ -based bulk system [12,45–47]. With further addition of Te, i.e., for  $x = 9$ ,  $\kappa$  increases but remains lower than the pristine  $\text{Sb}_2\text{Te}_3$ . It should be mentioned that  $\kappa$  consists of two independent contributions: one is the electronic component ( $\kappa_e$ ), and the other comes from lattice vibration ( $\kappa_L$ ). Heat conduction from electrons, holes, as well as bipolar conductivity can contribute to  $\kappa_e$  [48]. Bipolar conductivity comes into effect at high temperatures when minority carriers get activated and both majority and minority carriers contribute to electrical conductivity. However, such effects generally onset at high temperature. In addition, from  $S(T)$  data, no significant indication of minority carrier activation was observed. Furthermore, bipolar conduction often results in an upturn in  $\kappa(T)$  data at higher temperature, which is absent in our case [48]. Hence, the moderate temperature  $\kappa(T)$  data for the system under investigation reported here may be well characterized assuming only the majority carrier (holes here) contribution to  $\kappa_e$ . Here,  $\kappa_e$  can be estimated by the Wiedemann-Franz relationship:  $\kappa_e = LT/\rho$ , where  $L$  is the Lorenz number calculated via the single-band

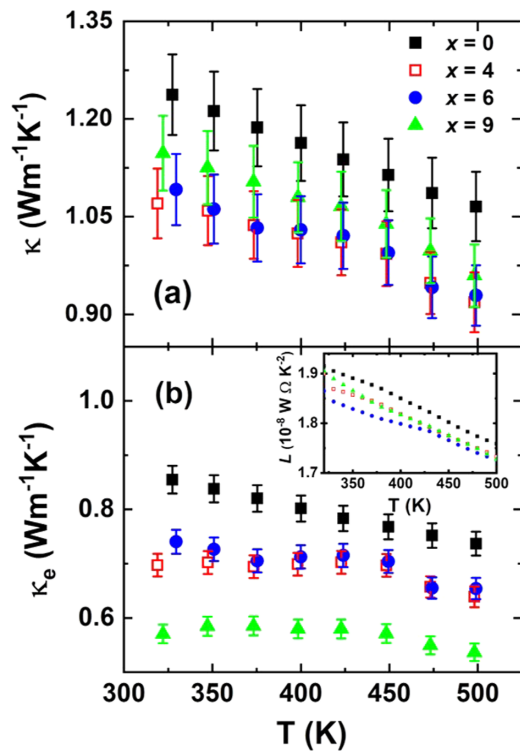


FIG. 7. Temperature dependence of (a) thermal conductivity  $\kappa$  and (b) electronic part of thermal conductivity  $\kappa_e$  for different mole percentage ( $x$ ) of Te in  $\text{Sb}_2\text{Te}_3/\text{Te}$  samples. Inset: Thermal variation of Lorenz number  $L$  for all samples.

parabolic (SPB) model [48]:

$$L = \frac{k_B^2 (1 + \lambda)(3 + \lambda)F_\lambda(\eta)F_{\lambda+2}(\eta) - (2 + \lambda)^2 F_{\lambda+1}(\eta)^2}{e^2 (1 + \lambda)^2 F_\lambda(\eta)^2}. \quad (2)$$

Here, it is assumed that carrier mobility is limited by acoustic phonon scattering, i.e.,  $\lambda = 0$ . It is quite justified to assume that this definition of  $L$  is appropriate for the present  $\text{Sb}_2\text{Te}_3$ -based structure system, where bipolar conduction is not playing a major role. This is further reflected in the  $L(T)$  curve [Inset of Fig. 7(b)], which decreases with increasing temperature for all samples. The lattice part of  $\kappa$ , i.e.,  $\kappa_L$  is estimated from the relation:  $\kappa = \kappa_e + \kappa_L$ . As shown in Fig. 8(a),  $\kappa_L$  for all samples decreases with increasing temperature. The observed trend in  $\kappa_L(T)$  data, at least in the temperature range of measurement, indicates the increase of phonon-phonon scattering with temperature. In crystalline solids,  $\kappa_L$  generally decays as  $T^{-1}$  in the temperature range where  $C_p$  is almost constant, and phonon-phonon scattering limits the phonon mean-free path [49]. From Fig. 8(a), it is observed that  $\kappa_L$  decreases with Te incorporation with a minimum  $\kappa_L$  value of  $0.28 \text{ Wm}^{-1} \text{ K}^{-1}$  at 500 K for  $x = 6$ . The maximum  $\sim 17\%$  decrease in  $\kappa_L$  as compared with the pristine sample was accomplished at the highest measured temperature for  $x = 6$ . At 500 K,  $\kappa_L$  values for samples with  $x = 4$  and 6 approach the theoretical minimum  $\kappa_L$  value for the  $\text{Sb}_2\text{Te}_3$ -based system ( $\kappa_{\min}$ ) estimated by the Cahill-Pohl model at the high-temperature ( $\kappa_{\min} \sim 0.31 \text{ Wm}^{-1} \text{ K}^{-1}$ ) limit

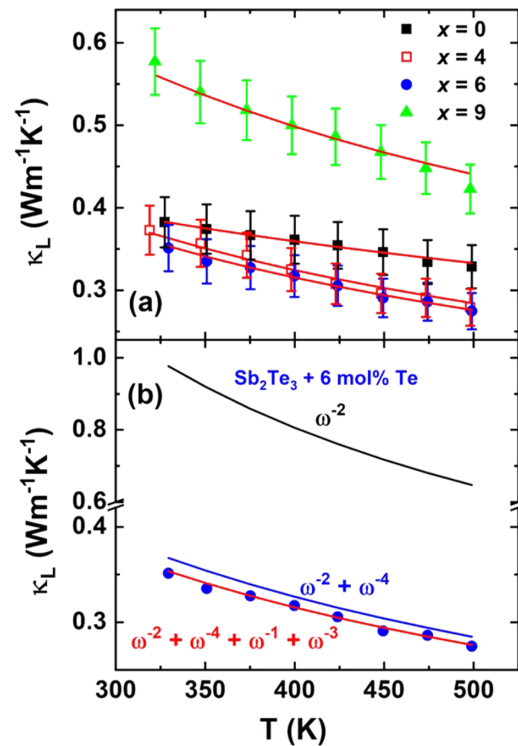


FIG. 8. (a) Temperature-dependent lattice thermal conductivity  $\kappa_L$  for  $\text{Sb}_2\text{Te}_3 + x \text{ mol\% Te}$  samples. Solid red lines are the best fits to Eq. (3) for  $x = 0, 4, 6,$  and  $9$ . (b) Contribution of different types of phonon scattering toward lattice thermal conductivity  $\kappa_L$  for a typical sample  $x = 6$  considering the frequency ( $\omega$ )-dependent terms successively for phonon relaxation time:  $\omega^{-2}$  for phonon-phonon (solid black line),  $\omega^{-4}$  for point defect (solid blue line), and  $\omega^{-1} + \omega^{-3}$  for dislocation scattering [solid red line in (b)].

[37,50]. However, it should be mentioned here that, during estimation of  $\kappa$ ,  $C_p$  is assumed to be temperature independent and limited by the Dulong-Petit value in the temperature range of measurement. It is noteworthy to mention that the Dulong-Petit law underestimates the experimentally measured heat capacity. At 300 K, the experimentally measured heat capacity is  $\sim 6\%$  higher than the heat capacity calculated using the Dulong-Petit law [18,37,45,51]. In reality, after 300 K,  $C_p$  increases with increasing temperature due to the presence of disorder and anharmonicity in the samples [18,37,45,51]. Nonetheless, the  $\kappa_L$  value reported here is one of the lowest reported so far for the  $\text{Sb}_2\text{Te}_3$  system [28,46,52–54]. For  $x = 9$ ,  $\kappa_L$  increases above the pristine sample and is reflected in the increasing trend in  $\kappa(T)$  data for the sample, despite having the lowest  $\kappa_e$  [Fig. 7]. Such an increase in  $\kappa$  for higher Te concentration ( $x = 9$ ) is probably due to higher  $\kappa$  value of Te than  $\text{Sb}_2\text{Te}_3$  [49,55].

Here,  $\kappa_L$  can be expressed as the sum of the contributions of heat-carrying phonons having a broad spectrum of frequencies ( $\omega$ ) [56]:  $\kappa_L = \int \kappa_s(\omega) d\omega$ , where spectral lattice thermal conductivity  $\kappa_s$  can be written as:  $\kappa_s(\omega) = C_p(\omega)v(\omega)\tau(\omega)$ . Here,  $C_p(\omega)$ ,  $v(\omega)$ , and  $\tau(\omega)$  are the spectral heat capacity of phonons, their velocity, and scattering time, respectively. While the specific heat at our relevant temperatures remains almost constant around the Dulong-Petit value, manipulation

TABLE I. Best fit values of temperature-independent parameters  $A_1$ ,  $B_1$ ,  $C_1$ , and  $D_1$  obtained by fitting lattice thermal conductivity  $\kappa_L$  data with Eq. (3) for  $x = 0, 4, 6$ , and  $9$  samples.

$x$	$A_1$	$B_1$	$C_1$	$D_1$
0	$0.776 \times 10^3$	9	$2.23 \times 10^4$	$1.13 \times 10^5$
4	$1.62 \times 10^3$	220	$0.21 \times 10^4$	$0.37 \times 10^5$
6	$1.65 \times 10^3$	250	$0.10 \times 10^4$	$0.28 \times 10^5$
9	$0.754 \times 10^3$	255	$0.07 \times 10^4$	$0.23 \times 10^5$

of the scattering time of phonons has been proven to be an effective strategy to lower  $\kappa_L$  [8]. Using the phonon transport model based on phonon relaxation time,  $\kappa_L(T)$  can be calculated using the following equation [57]:

$$\kappa_L(T) = \frac{k_B}{2\pi^2 v} \left( \frac{k_B T}{h} \right)^3 \int_0^{\theta_D/T} \tau_{\text{tot}} \frac{x^4 e^x}{(e^x - 1)^2} dx, \quad (3)$$

where  $x = \hbar\omega/k_B T$ ;  $v$ ,  $\theta_D$ , and  $\tau_{\text{tot}}$  are the average sound speed ( $= 1900$  m/s from Ref. [45]), Debye temperature, and the total relaxation time, respectively. Here,  $\tau_{\text{tot}}$  consists of different frequency- and temperature-dependent relaxation times related to different types of phonon scattering, viz., phonon-phonon Umklapp scattering due to lattice anharmonicity ( $\tau_U$ ), phonon scattering by zero-dimensional point defects ( $\tau_{PD}$ ), one-dimensional dislocation ( $\tau_{DS}$ ,  $\tau_{DC}$ ), and two-dimensional (2D) interfaces including grain boundary scattering ( $\tau_{\text{Inter}}$ ) [8]. It is noteworthy to mention that 2D interfaces scatter low-frequency phonons ( $\tau_{\text{Inter}} \sim \omega^0$ ). As at low temperatures, heat carrying phonons usually have low frequency, phonon scattering by 2D interfaces has a significant effect on  $\kappa_L$  at low temperature [8]. In the temperature range of investigation in our case [57],

$$\begin{aligned} \tau_{\text{tot}}^{-1} &= \tau_U^{-1} + \tau_{PD}^{-1} + \tau_{DC}^{-1} + \tau_{DS}^{-1} \\ &= A_1 \omega^2 T + B_1 \omega^2 + C_1 \omega^3 + D_1 \omega. \end{aligned} \quad (4)$$

We assume that  $A_1$ ,  $B_1$ ,  $C_1$ , and  $D_1$  are temperature-independent parameters. An attempt has been made to fit the  $\kappa_L$  curves for  $x = 0, 4, 6$ , and  $9$  with Eq. (3), which are depicted in Fig. 8(a). The best fit parameters for all relevant samples are listed in Table I. It is revealed that phonon-phonon Umklapp scattering increases for Te-incorporated samples. The anharmonic nature of chemical bonds increases in the  $\text{Sb}_2\text{Te}_3$  matrix additionally doped with Te atoms. Increasing strain on the  $\text{Sb}_2\text{Te}_3$  matrix with Te addition, as divulged by Rietveld analysis of the XRD patterns, leads to fluctuation of effective force constant between the atoms and hence shortens the phonon relaxation time [58]. Increase of the  $B_1$  parameter with Te inclusion indicates that, during synthesis, extra Te creates additional extrinsic point defects in the host matrix, and hence, scattering of high-frequency phonons is increased in  $x = 4, 6$ , and  $9$  samples. As demonstrated earlier through the increase of lattice parameters of  $\text{Sb}_2\text{Te}_3$  in the Te-impurity-incorporated samples and  $n_H$  measurement, Te incorporation decreases  $V_{\text{Te}}^{\bullet\bullet}$ -type defects. It is noteworthy to mention that the presence of vacancy in the lattice often leads to dislocations in the crystals [57]. Thus, in  $x = 4, 6$ , and  $9$  samples having lower Te vacancy in the host matrix, scattering of midfrequency phonons should be less than in the pristine

sample. This is confirmed by the lower values of  $C_1$  and  $D_1$  (Table I) of these samples. However, having a smaller value of total  $\tau$  ensures that  $\kappa_L$  drops to a lower value for  $x = 4$  and  $6$  than the pristine sample. Contribution of different types of phonon scattering toward lowering of  $\kappa_L$  has been demonstrated in Fig. 8(b) for a typical sample of  $x = 6$ . However, this plausible explanation of phonon scattering by defects of different dimensionalities in the relevant samples should be confirmed after further detailed investigation of microscopic structure along with the phonon spectra of the samples.

### E. Discussions: Impact on the TE figure of merit

First, the observed change in charge carrier concentration with the increasing amount of extra Te should be discussed in the defect description often used in  $\text{Sb}_2\text{Te}_3$ , as the presence of different types of defects often affects  $n_H$ . It should be mentioned that  $\text{Sb}_2\text{Te}_3$  contains native defects like  $V_{\text{Te}}^{\bullet\bullet}$ ,  $\text{Sb}'_{\text{Te}}$ , and  $V_{\text{Sb}}^{\bullet\bullet}$  [24]. Due to the large difference in the saturation vapor pressure of Sb and Te,  $V_{\text{Te}}^{\bullet\bullet}$  are created in  $\text{Sb}_2\text{Te}_3$  during the growth process. The formation energy of the  $V_{\text{Te}}^{\bullet\bullet}$  is higher than that of the antisite defect [59,60]. Hence, superstoichiometric Sb atoms make their way to vacant Te sites, and an antisite defect of  $\text{Sb}'_{\text{Te}}$  type is formed. Defect density, viz.,  $V_{\text{Te}}^{\bullet\bullet}$  and  $\text{Sb}'_{\text{Te}}$  determines  $n_H$ . However, the presence of extra Te during synthesis (for  $x = 4, 6$ , and  $9$ ) suppresses formation of  $V_{\text{Te}}^{\bullet\bullet}$ . In Te-rich conditions,  $V_{\text{Sb}}^{\bullet\bullet}$ , whose formation energy is the lowest, along with  $V_{\text{Te}}^{\bullet\bullet}$ , plays a dominant role in determining  $n_H$  [24]. It is noteworthy to mention here that defect concentration often depends on the synthesis condition. The Hall concentration for the present set of samples under investigation is higher than some examples reported in the literature for  $\text{Sb}_2\text{Te}_3$ -based system [12,14,27,42]. The annealing protocol and corresponding temperatures used in different stages of sample preparation probably give rise to higher defect density in our present samples. For  $\text{Sb}_2\text{Te}_3/\text{Te}$  samples, extra Te was present during synthesis of  $\text{Sb}_2\text{Te}_3$ . Hence, density of  $V_{\text{Te}}^{\bullet\bullet}$  decreases, and  $V_{\text{Sb}}^{\bullet\bullet}$  increases. Thus,  $n_H$  decreases initially for the  $\text{Sb}_2\text{Te}_3/\text{Te}$  system with Te incorporation. However, with further increase of Te concentration, the contribution of holes from elemental Te increases the carrier concentration in the system [49], which is reflected in higher  $n_H$  for  $x \geq 6$  (Fig. 4).

Nevertheless, our results show an  $S$  variation with  $x$  that does not follow the trend of  $n_H$  of the samples as per Eq. (1). In that case, variation of  $m^*$  comes into play. Here,  $m^*$  depends on band effective mass ( $m_b^*$ ) and the number of equivalent degenerate valleys ( $N_V$ ) of the samples and is expressed as  $m^* = N_V^{2/3} m_b^*$  [41]. It should be mentioned here that the change in  $m_b^*$  is reflected through change in mobility, and hence, an attempt has been made to estimate the weighted mobility ( $\mu_W$ ) of the synthesized samples ( $x = 0, 4, 6$ , and  $9$ ). Here,  $\mu_W$  is calculated based on the SPB model using the expression [48,61,62]:

$$\mu_W = \frac{3\sigma}{8\pi e F_0(\eta)} \left( \frac{h^2}{2m_e k_B T} \right)^{3/2}, \quad (5)$$

where  $m_e$  denotes electronic mass. Here,  $\sigma (= 1/\rho)$  and  $F_0(\eta)$  are obtained from the measured  $\rho(T)$  and  $S(T)$  data. As shown



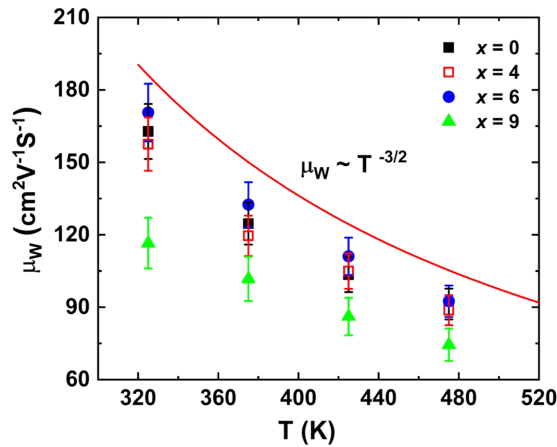


FIG. 9. Thermal variation of weighted mobility  $\mu_W$  for  $\text{Sb}_2\text{Te}_3/\text{Te}$  composite systems. The solid red line shows roughly the temperature dependence of  $\mu_W$  ( $\sim T^{-3/2}$ ).

in Fig. 9, over the whole temperature region,  $\mu_W$  takes almost a similar value for  $x = 0, 4,$  and  $6$ . Enhanced texture due to incorporation of Te, as demonstrated by Rietveld analysis of the XRD patterns, prevents deterioration of  $\mu_W$  for  $x = 4$  and  $6$  [15–17]. For each of these samples,  $\mu_W$  decreases with temperature and follows a  $\mu_W \sim T^{-3/2}$  power law due to the unchanged dominant acoustic phonon scattering mechanism [63]. It is noteworthy to mention here that almost the same value of  $\mu_W$  for  $x = 0, 4,$  and  $6$  indicates that there is no significant flattening or sharpening of the band with Te incorporation and  $m_b^*$  is similar for all samples under consideration. However, different  $\mu_W$  values throughout the temperatures for  $x = 9$  indicate a change in  $m_b^*$  for the sample. Thus, the anticipated variation in  $m^*$  for  $x = 0, 4,$  and  $6$  originates from the change in  $N_V$ . Variation in  $m^*$  due to change in  $N_V$  has also been reported by Chen *et al.* [61] for the Bi-incorporated SnTe–MnTe alloy. Change in  $N_V$  is usually reflected in the electronic band structure through convergence or divergence of the bands having very close energy. Thus, to explain the observed variation of  $m^*$  through change in  $N_V$ , a multiband transport model must be assumed. It should be mentioned here that significant variation of  $n_H$  with  $T$  as depicted in Fig. 4 also supports the fact that more than one band is playing a role in determining transport properties in our system. In addition, an attempt has been made to plot the magnetoresistance (MR) ratio as a function of  $H/\rho(0)$  (Kohler plot), where  $H$  and  $\rho(0)$  are magnetic field and electrical resistivity at zero field, respectively (Fig. SM2 in the Supplemental Material [36]). As indicated by the plot, for each sample, MR data at different temperatures do not collapse to a single universal curve, suggesting that electronic transport properties are dominated by more than one type of carrier [64].

Earlier reports of band structure by first-principles calculations revealed the multivalley nature of the band for the  $\text{Sb}_2\text{Te}_3$  system [52]. Schematically, it can be represented by an upper valence band (UVB) of light holes, lower valence band (LVB) of heavy holes, upper conduction band having heavy electrons, and lower conduction band containing light electrons, as shown by Kulbachinskii *et al.* [11]. The reported

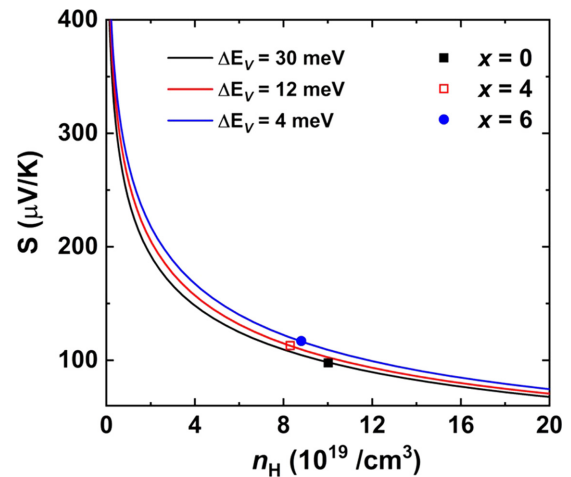


FIG. 10. Experimental  $S$  vs  $n_H$  data at 300 K of  $\text{Sb}_2\text{Te}_3 + x$  mol % Te ( $x = 0, 4,$  and  $6$ ) with the theoretically calculated Pisarenko curve by varying energy gap between light and heavy hole valence bands of  $\text{Sb}_2\text{Te}_3$ .

value of the energy separation ( $\Delta E_V$ ) between UVB and LVB for the  $\text{Sb}_2\text{Te}_3$  system at 4.2 K is  $\sim 150$  meV, as determined from Shubnikov–de Haas measurements [65]. However, Kim *et al.* [66] estimated  $\Delta E_V$  to be 10 meV at 300 K. On the other hand, according to Kohler *et al.* [67],  $\Delta E_V$  for the  $(\text{Bi}_{1-x}\text{Sb}_x)_2\text{Te}_3$  ( $0 < x < 1$ ) system is of the order of 20–30 meV. We have attempted to simulate the experimentally measured room-temperature  $S$  vs  $n_H$  data by the theoretically obtained Pisarenko curve with the double valence band model (Fig. 10) [53]. The details are provided in the Supplemental Material [36]. From Fig. 10, for  $x = 0$ , the experimental data fit well with  $\Delta E_V = 30$  meV. However, the experimental  $S$  vs  $n_H$  data for  $x = 4$  and  $6$  lie above the curve [black line in Fig. 10]. It indicates that increase of  $m^*$  by convergence of UVB and LVB can be one of the reasons. To validate this point, an attempt is made to simulate measured  $S$  vs  $n_H$  data for  $x = 4$  and  $6$  thorough the Pisarenko curve with the double valence band model by varying the energy gap  $\Delta E_V$  between two valence bands. A gradual decrease of  $\Delta E_V$  from 30 meV for  $x = 0$  to 12 and 4 meV for  $x = 4$  and  $6$ , respectively, confirms that, with increase of  $x$ , UVB and LVB gradually converge. However, as discussed earlier, a similar statement cannot be made for  $x = 9$ , as Fig. 9 indicates different  $m_b^*$  for the sample. Though any band structure is compound specific, still, the example of SnTe and GeTe can be cited, where convergence of valence bands has already been reported to play a positive role in enhancing  $S$  [53,54]. In our case, larger  $S$  for  $x = 4$  and  $6$  can be attributed to valence band convergence. Here, we should mention that data in the literature are lacking related to the synergistic effect of such a manipulation of the electronic structure as well as charge carrier concentration in  $\text{Sb}_2\text{Te}_3$ -based TE material.

For comparing TE performance among samples with different  $n_H$ ,  $\mu_W$  and  $\kappa_L$  data can be utilized. Using the effective mass model [68], the material quality factor  $B$  is calculated to estimate the optimal TE performance for the

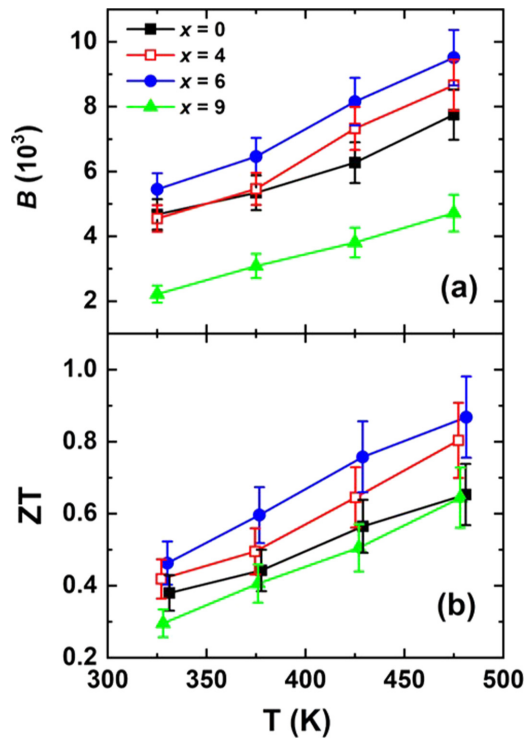


FIG. 11. Thermal variation of (a) quality factor  $B$  and (b) thermoelectric figure of merit  $ZT$  for  $\text{Sb}_2\text{Te}_3/\text{Te}$  samples with different mole percentage ( $x$ ) of Te. The unit of  $B$  is in  $\text{cm}^2 \text{V}^{-1} \text{s}^{-1} / \text{Wm}^{-1} \text{K}^{-1}$ . Lines connecting the data points are provided as guides to the eye.

materials [62]:

$$B = 9 \frac{\mu_W}{\kappa_L} \left( \frac{T}{300} \right)^{5/2}. \quad (6)$$

The estimated values of  $B$  as plotted in Fig. 11(a) elucidate that it increases with temperature for all samples, with  $B$  values being higher for  $x = 4$  and  $6$  than its pristine counterpart. Here, the  $x = 6$  sample, having the highest  $B$  value, exhibits a 16 and 23% increase in  $B$  at 325 and 500 K, respectively. Such an increase in  $B$  for these samples results from the fact that incorporating the Te phase into the  $\text{Sb}_2\text{Te}_3$  matrix not only favorably maintains the carrier mobility but also suppresses  $\kappa_L$ . Consequently, an increasing  $ZT$  with temperature for all samples and the highest  $ZT$  for  $x = 6$  is observed

[Fig. 11(b)]. A high value of  $ZT \sim 0.87$  at 480 K is achieved for  $\text{Sb}_2\text{Te}_3 + 6 \text{ mol } \% \text{ Te}$ , which is  $\sim 33\%$  higher than its pristine counterpart. The high  $ZT$  value of our synthesized  $\text{Sb}_2\text{Te}_3/\text{Te}$  sample can be attributed to high  $S$  and low  $\kappa$ , obtained through strong phonon scattering.

#### IV. CONCLUSIONS

In this paper, a detailed systematic investigation of TE performance of the Te-impurity-based  $\text{Sb}_2\text{Te}_3$  system has been performed. It is observed that, in addition to serving the advantages of being a second phase in the matrix, the presence of Te also helps in tuning  $n_H$  toward achieving enhanced TE performance. With a favorable  $n_H$ , a relative decrease in energy offset between UVB and LVB ensures a higher  $S$  for  $x = 4$  and  $6$ . Moreover, Te addition helps to scatter phonons, and a low  $\kappa_L$  of  $\sim 0.28 \text{ Wm}^{-1} \text{K}^{-1}$  around the theoretical minimum  $\kappa$  ( $\kappa_{\min}$ ) has been reported. Our analysis reveals that, although there is a decrease in dislocation-induced mid-frequency phonon scattering, high-frequency phonons are scattered significantly by newly formed Te-based point defects in the matrix of  $\text{Sb}_2\text{Te}_3/\text{Te}$  structures. As a result of such a beneficial effect of Te addition,  $\sim 33\%$  increase in  $ZT$  at 480 K ( $ZT = 0.87$ ) is accomplished in the  $\text{Sb}_2\text{Te}_3/\text{Te}$  sample ( $x = 6$ ). It is very likely that  $ZT$  may be further increased through optimizing  $n_H$  and controlling the texture of the  $x = 6$  sample, which should be investigated in the future.

#### ACKNOWLEDGMENTS

This paper is supported by UGC DAE CSR, Kolkata Centre, Government of India (Project Reference No. UGC-DAE-CSR-KC/CRS/19/MS02/0939) and the Inter-University Accelerator Centre, New Delhi, Government of India (Project Code No. UFR-65307). P. Singha is thankful to UGC DAE CSR, Kolkata Centre, Government of India, for providing him a research fellowship. Subarna Das is grateful to UGC, Government of India, for providing financial assistance in the form of a senior research fellowship and acknowledges the support received through the Raman-Charpak Fellowship 2019 jointly funded by the Department of Science and Technology, Government of India, and the French Institute in India, French Embassy in India, Ministry for Europe and Foreign Affairs, Government of France.

- [1] G. J. Snyder and E. S. Toberer, *Nat. Mater.* **7**, 105 (2008).
- [2] K. Behnia, *Fundamentals of Thermoelectricity* (Oxford University Press, Oxford, 2015).
- [3] T. Pandey, L. Lindsay, B. C. Sales, and D. S. Parker, *Phys. Rev. Mater.* **4**, 045403 (2020).
- [4] J. P. Heremans, V. Jovicic, E. S. Toberer, A. Saramat, K. Kurosaki, A. Charoenphakdee, S. Yamanaka, and G. J. Snyder, *Science* **321**, 554 (2008).
- [5] Y. Pei, X. Shi, A. LaLonde, H. Wang, L. Chen, and G. J. Snyder, *Nature (London)* **473**, 66 (2011).
- [6] W. Li, Z. Chen, S. Lin, Y. Chang, B. Ge, Y. Chen, and Y. Pei, *J. Materiomics* **1**, 307 (2015).
- [7] H. Jang, S. Abbey, W. H. Nam, B. Frimpong, C. V. Nguyen, S.-J. Joo, H. S. Shin, J. Y. Song, E. N. Cho, M. Kim, Y. S. Jung, and M.-W. Oh, *J. Mater. Chem. A* **9**, 4648 (2021).
- [8] Z. Chen, X. Zhang, and Y. Pei, *Adv. Mater.* **30**, 1705617 (2018).
- [9] C. Zhu, J. Zhang, H. Ming, X. Lou, L. Huang, T. Chen, B. Zhang, D. Li, H. Xin, and X. Qin, *Appl. Phys. Lett.* **117**, 042105 (2020).
- [10] C. Gayner and Y. Amouyal, *Adv. Funct. Mater.* **30**, 1901789 (2020).
- [11] V. D. Blank, S. G. Buga, V. A. Kulbachinskii, V. G. Kytin, V. V. Medvedev, M. Y. Popov, P. B. Stepanov, and V. F. Skok, *Phys. Rev. B* **86**, 075426 (2012).

- [12] M. Ahmad, K. Agarwal, N. Kumari, and B. R. Mehta, *Appl. Phys. Lett.* **111**, 023904 (2017).
- [13] Z. Xu, H. Wu, T. Zhu, C. Fu, X. Liu, L. Hu, J. He, J. He, and X. Zhao, *NPG Asia Materials* **8**, e302 (2016).
- [14] I. T. Witting, J. A. Grovogui, V. P. Dravid, and G. J. Snyder, *J. Materiomics* **6**, 532 (2020).
- [15] L. D. Zhao, B. P. Zhang, J. F. Li, H. L. Zhang, and W. S. Liu, *Solid State Sci.* **10**, 651 (2008).
- [16] X. Yan, B. Poudel, Y. Ma, W. S. Liu, G. Joshi, H. Wang, Y. C. Lan, D. Z. Wang, G. Chen, and Z. F. Ren, *Nano Lett.* **10**, 3373 (2010).
- [17] L. P. Hu, X. H. Liu, H. H. Xie, J. J. Shen, T. J. Zhu, and X. B. Zhao, *Acta Mater.* **60**, 4431 (2012).
- [18] D. Das, S. Das, P. Singha, K. Malik, A. K. Deb, A. Bhattacharya, V. A. Kulbachinskii, R. Basu, S. Dhara, S. Bandyopadhyay, and A. Banerjee, *Phys. Rev. B* **96**, 064116 (2017).
- [19] C. Dun, C. A. Hewitt, Q. Li, J. Xu, D. C. Schall, H. Lee, Q. Jiang, and D. L. Carroll, *Adv. Mater.* **29**, 1700070 (2017).
- [20] F. Rieger, V. Roddatis, K. Kaiser, G. Bendt, S. Schulz, and C. Jooss, *Phys. Rev. Materials* **4**, 025402 (2020).
- [21] G. S. Nolas, J. Sharp, and H. J. Goldsmid, *Thermoelectric Basic Principles and New Materials Developments* (Springer, Berlin, Heidelberg, 2001).
- [22] H. Zhang, C.-X. Liu, X.-L. Qi, X. Dai, Z. Fang, and S.-C. Zhang, *Nat. Phys.* **5**, 438 (2009).
- [23] P. Lošták, Č. Drašar, J. Horák, Z. Zhou, J. S. Dyck, and C. Uher, *J. Phys. Chem. Solids* **67**, 1457 (2006).
- [24] D. West, Y. Y. Sun, H. Wang, J. Bang, and S. B. Zhang, *Phys. Rev. B* **86**, 121201(R) (2012).
- [25] D.-K. Ko, Y. Kang, and C. B. Murray, *Nano Lett.* **11**, 2841 (2011).
- [26] W. Zheng, P. Bi, H. Kang, W. Wei, F. Liu, J. Shi, L. Peng, Z. Wang, and R. Xiong, *Appl. Phys. Lett.* **105**, 023901 (2014).
- [27] Y. Zhang, M. L. Snedaker, C. S. Birkel, S. Mubeen, X. Ji, Y. Shi, D. Liu, X. Liu, M. Moskovits, and G. D. Stucky, *Nano Lett.* **12**, 1075 (2012).
- [28] M. H. Lee, K.-R. Kim, J.-S. Rhyee, S.-D. Park, and G. J. Snyder, *J. Mater. Chem. C* **3**, 10494 (2015).
- [29] Z. Zhang, Y. Wu, H. Zhang, Z. Zeng, and Z. Hu, *J. Mater. Sci: Mater. Electron.* **26**, 1619 (2015).
- [30] H. Peng, N. Kioussis, and G. J. Snyder, *Phys. Rev. B* **89**, 195206 (2014).
- [31] C. Dun, C. A. Hewitt, H. Huang, D. S. Montgomery, J. Xu, and D. L. Carroll, *Phys. Chem. Chem. Phys.* **17**, 8591 (2015).
- [32] J. G. M. Van Berkum, G. J. M. Sprong, T. de Keijser, R. Delhez, and E. J. Sonneveld, *Powder Diffr.* **10**, 129 (1995).
- [33] L. Lutterotti, S. Matthies, and H. R. Wenk, in *Proceedings of ICOTOM14*, edited by J. A. Spunar (National Research Council of Canada, Ottawa, 1999), p.1599; IUCr: Newsl. CPD **21**, 14 (1999).
- [34] N. C. Popa, *J. Appl. Cryst.* **31**, 176 (1998).
- [35] E. Zolotoyabko, *J. Appl. Cryst.* **42**, 513 (2009).
- [36] See Supplemental Material at <http://link.aps.org/supplemental/10.1103/PhysRevMaterials.6.035401> for details of XRD patterns after Rietveld refinement along with corresponding refinement parameters, phase fraction of  $\text{Sb}_2\text{Te}_3$  and Te impurity, and Kohler and Piseranko plots based on two valence band model.
- [37] S. Das, P. Singha, V. A. Kulbachinskii, V. G. Kytin, G. Das, S. Janaky, A. K. Deb, S. Mukherjee, A. Maignan, S. Hebert, R. Daou, C. Narayana, S. Bandyopadhyay, and A. Banerjee, *J. Materiomics* **7**, 545 (2021).
- [38] D. Das, K. Malik, A. K. Deb, S. Dhara, S. Bandyopadhyay, and A. Banerjee, *J. Appl. Phys.* **118**, 045102 (2015).
- [39] S. Mukherjee, O. E. Femi, R. Chetty, K. Chattopadhyay, S. Suwas, and R. C. Mallik, *Appl. Surf. Sci.* **449**, 805 (2018).
- [40] D. M. Rowe, *Thermoelectrics Handbook: Macro to Nano* (CRC Press, New York, 2006).
- [41] Y. Pei, H. Wang, and G. J. Snyder, *Adv. Mater.* **24**, 6125 (2012).
- [42] Z. Wu, X. Chen, E. Mu, Y. Liu, Z. Che, C. Dun, F. Sun, X. Wang, Y. Zhang, and Z. Hu, *Adv. Electron. Mater.* **6**, 1900735 (2019).
- [43] D. Das, K. Malik, A. K. Deb, V. A. Kulbachinskii, V. G. Kytin, S. Chatterjee, D. Das, S. Dhara, S. Bandyopadhyay, and A. Banerjee, *Europhys. Lett.* **113**, 47004 (2016).
- [44] P. Dutta, D. Bhoi, A. Midya, N. Khan, P. Mandal, S. S. Samatham, and V. Ganesan, *Appl. Phys. Lett.* **100**, 251912 (2012).
- [45] D. Bessas, I. Sergueev, H.-C. Wille, J. Perbon, D. Ebling, and R. P. Hermann, *Phys. Rev. B* **86**, 224301 (2012).
- [46] N.-W. Park, W.-Y. Lee, J.-E. Hong, T.-H. Park, S.-G. Yoon, H. Im, H. S. Kim, and S.-K. Lee, *Nanoscale Res. Lett.* **10**, 20 (2015).
- [47] S. Das, P. Singha, A. K. Deb, S. C. Das, S. Chatterjee, V. A. Kulbachinskii, V. G. Kytin, D. A. Zinoviev, N. V. Maslov, S. Dhara, S. Bandyopadhyay, and A. Banerjee, *J. Appl. Phys.* **125**, 195105 (2019).
- [48] A. F. May, E. S. Toberer, A. Saramat, and G. J. Snyder, *Phys. Rev. B* **80**, 125205 (2009).
- [49] S. Lin, W. Li, Z. Chen, J. Shen, B. Ge, and Yanzhong Pei, *Nat. Commun.* **7**, 10287 (2016).
- [50] P. Singha, S. Das, V. A. Kulbachinskii, V. G. Kytin, A. S. Apreleva, D. J. Voneshen, T. Guidi, A. V. Powell, S. Chatterjee, A. K. Deb, S. Bandyopadhyay, and A. Banerjee, *J. Appl. Phys.* **129**, 055108 (2021).
- [51] D. Das, K. Malik, S. Das, P. Singha, A. K. Deb, V. A. Kulbachinskii, R. Basu, S. Dhara, A. Dasgupta, S. Bandyopadhyay, and A. Banerjee, *AIP Advances* **8**, 125119 (2018).
- [52] G. Wang and T. Cagin, *Phys. Rev. B* **76**, 075201 (2007).
- [53] Q. Zhang, B. Liao, Y. Lan, K. Lukas, W. Liu, K. Esfarjani, C. Opeil, D. Broido, G. Chen, and Z. Ren, *Proc. Natl. Acad. Sci. USA* **110**, 13261 (2013).
- [54] D. Sarkar, T. Ghosh, A. Banik, S. Roychowdhury, D. Sanyal, and K. Biswas, *Angew. Chem. Int. Ed.* **59**, 11115 (2020); Y. Feng, J. Li, Y. Li, T. Ding, C. Zhang, L. Hu, F. Liu, W. Ao, and C. Zhang, *J. Mater. Chem. A* **8**, 11370 (2020).
- [55] Y. Wu, Q. Zhang, F. Liu, T. Fang, T. Zhu, and X. Zhao, *Adv. Electron. Mater.* **6**, 2000038 (2020).
- [56] E. S. Toberer, A. Zevkink, and G. J. Snyder, *J. Mater. Chem.* **21**, 15843 (2011).
- [57] Z. Chen, B. Ge, W. Li, S. Lin, J. Shen, Y. Chang, R. Hanus, G. J. Snyder, and Y. Pei, *Nat. Commun.* **8**, 13828 (2017).
- [58] Y. Wu, Z. Chen, P. Nan, F. Xiong, S. Lin, X. Zhang, Y. Chen, L. Chen, B. Ge, and Y. Pei, *Joule* **3**, 1276 (2019).
- [59] J. Horák, K. Čermák, and L. Koudelka, *J. Phys. Chem. Solids* **47**, 805 (1986).

- [60] T. Thonhauser, G. S. Jeon, G. D. Mahan, and J. O. Sofo, *Phys. Rev. B* **68**, 205207 (2003).
- [61] Z. Chen, J. Tang, X. Guo, F. Zhang, M. Tang, F. Xiong, Y. Chen, and R. Ang, *Appl. Phys. Lett.* **116**, 193902 (2020).
- [62] Y. Xiao, D. Wang, Y. Zhang, C. Chen, S. Zhang, K. Wang, G. Wang, S. J. Pennycook, G. J. Snyder, H. Wu, and L.-D. Zhao, *J. Am. Chem. Soc.* **142**, 4051 (2020).
- [63] K. Borkowski and J. Przyłuski, *Mater. Res. Bull.* **22**, 381 (1987).
- [64] Z. Hou, B. Yang, Y. Wang, B. Ding, X. Zhang, Y. Yao, E. Liu, X. Xi, G. Wu, Z. Zeng, Z. Liu, and W. Wang, *Sci. Rep.* **6**, 23807 (2016).
- [65] A. von Middendorff, K. Dietrich, and G. Landwehr, *Solid State Commun.* **13**, 443 (1973).
- [66] H.-S. Kim, N. A. Heinz, Z. M. Gibbs, Y. Tang, S. D. Kang, and G. J. Snyder, *Mater. Today* **20**, 452 (2017).
- [67] H. Kohler and A. Freudenberger, *Phys. Stat. Solidi B* **84**, 195 (1977).
- [68] A. Zevalkink, D. M. Smiadak, J. L. Blackburn, A. J. Ferguson, M. L. Chabinyk, O. Delaire, J. Wang, K. Kovnir, J. Martin, L. T. Schelhas, T. D. Sparks, S. D. Kang, M. T. Dylla, G. J. Snyder, B. R. Ortiz, and E. S. Toberer, *Appl. Phys. Rev.* **5**, 021303 (2018).